Probing the impact of advanced melting and advanced adsorption phenomena on the accuracy of pore size distributions from cryoporometry and adsorption using NMR relaxometry and diffusometry

Elenica Shiko[a], Karen J. Edler[b], John P. Lowe[b], and Sean P. Rigby[c,*]

[a]*Department of Chemical Engineering, University of Bath, Claverton Down, Bath, BA2 7AY, U.K.*

[b]*Department of Chemistry, University of Bath, Claverton Down, Bath, BA2 7AY, U.K.*

[c]*Department of Chemical and Environmental Engineering, University of Nottingham, University Park, Nottingham, NG7 2RD, U.K.*

*Corresponding author

Current address: Department of Chemical and Environmental Engineering, University of Nottingham, U.K.

Telephone No.: +44 (0) 115 951 4078

Email: enzspr@exmail.nottingham.ac.uk

Abstract

The accuracy of pore size distributions (PSD) obtained from gas adsorption and cryoporometry is compromised by the presence of advanced adsorption and advanced melting effects, respectively. In order to improve PSD accuracy, it is necessary to know the extent of such effects. In this work cryoporometry and adsorption have been combined to study the onset of advanced melting effects in a sample partially-saturated with different volumes of condensate, in turn, by pre-equilibration with different vapour pressures of adsorbate. NMR relaxometry and diffusometry have been used to independently study the size and connectivity of adsorbed liquid ganglia at different molten fractions. It has been found that the onset of significant advanced melting coincided with abrupt changes in levels of individual pore-filling and ganglia inter-connections determined by NMR. These findings also highlighted where significant advanced adsorption processes were occurring, where larger pores were being filled with condensate before smaller pores. These studies have enabled the critical pores governing the advanced processes to be identified, and the likely errors in PSDs arising from advanced effects to be quantified.

Keywords: Adsorption; Catalyst support; Diffusion; NMR cryoporometry; Phase change; Porous media

INTRODUCTION

The pore size distribution (PSD) is a key descriptor for characterising the void space of a porous solid, such as a heterogeneous catalyst [1]. The PSD can be the main factor determining important features of porous solids, such as the overall activity, or coking-resistance, of a heterogeneous catalyst. Hence, it is important to obtain an accurate determination of the PSD. A number of different techniques, such as gas adsorption, mercury porosimetry, NMR cryoporometry, DSC thermoporometry, and NMR relaxometry can be used to determine pore size information. Each of these techniques depends on a different physical process, and relies upon a different theory, and accompanying set of auxiliary assumptions, with which to transform raw experimental characterisation data into a PSD.

The gas adsorption experiment consists of the initial evacuation of a porous sample, to remove any contaminating volatiles, and then the progressive application of step-wise increases in the imposed pressure of an adsorbate, such as nitrogen [1]. For nitrogen at 77 K, the adsorption process, in a given pore, is generally thought to consist of initial build-up of adsorbed layers on the pore walls, followed by pore-filling by capillary condensation at the particular pressure characteristic of the specific pore size, as given by the Kelvin equation [1]. For a porous solid possessing a distribution in pore sizes, the probability density function of pore size weighted by pore volume (usually simply called the PSD) can be obtained from the nitrogen adsorption isotherm using an algorithm such as the Barrett-Joyner-Halenda (BJH) method [2]. This algorithm makes the assumption that pores of different sizes are thermodynamically independent. This is equivalent to treating the individual ‘pores’ within an irregular, interconnected void space as if they were located within a hypothetical parallel pore bundle. Even assuming it is possible to obtain a physically meaningful definition of a ‘single pore’ within an irregular, interconnected void space, this assumption neglects the possibility of interactions between neighbouring pores, or even over much larger length-scales. Alternative methods, such as non-local density functional theory (NLDFT) [3], improve on the pore-scale physics of the phase transition in a single pore but subsequent calculations of pore size distributions still make the same assumptions regarding thermodynamically independent pores as with the BJH method.

From considerations of basic adsorption theory, involving the Kelvin equation, it is possible to deduce that cooperative pore-pore interaction phenomena will occur during adsorption [4]. It proposed that, for a through (open) ink-bottle pore geometry, if the radius of the two shielding pore necks is greater than half that of the intermediate pore body then all will fill at the same pressure. In this case, the pressure required is equivalent to that given by the Cohan [5] equation for a cylindrical meniscus in the pore neck. This is because once condensate has filled the pore neck, filling of the pore body may then proceed via ingress of the, now hemispherical, meniscus from the end of the pore neck. If the pore neck radius is over half that of the pore body, then the pressure for condensation within the pore body, for a hemispherical meniscus, is exceeded by the pressure required to condense in the neck with a cylindrical meniscus. This process is known as the 'advanced adsorption' or 'advanced condensation' effect [6]. Grand canonical Monte-Carlo (GCMC) simulations [7] of argon adsorption in model, unconnected pores possessing corrugations have confirmed the aformentioned general picture as originally proposed by de Boer [4]. Mean-field density functional theory (MFDFT) simulations of adsorption, in disordered models for silica aerogels, have shown that an initially localized condensation event can trigger further collective condensation in neighbouring cavities, such that the independent pore model is completely inappropriate for these materials [8].

Cooperative effects during adsorption have also been observed directly during experiments on the capillary condensation of hexane within model funnel-, and ink-bottle, shaped pores, within anodized alumina, using optical interferometry [9,10]. By employing subsequent adsorption of argon, following initial water adsorption and freezing, Giacobbe *et al.* [11] found that appreciable pore-filling, with water, occurred in pores with a radius of 4 nm at the same time that pores of radii 1.8-2.3 nm were, themselves, being filled within a Vycor sample. However, this work used adsorption itself to study an adsorbed phase. In contrast, Hitchcock *et al*. [12] used NMR relaxometry to independently study the adsorbed phase, and have observed long-range (>100 μm) cooperative effects during water adsorption, within mesoporous silica, using magnetic resonance imaging (MRI), that may mean that PSDs can be as much as 500% out from the real pore size.

Cryoporometry is a technique of pore size determination based upon the depression of the freezing and melting points of fluids imbibed within confined geometries [13,14]. Fluids imbibed within smaller pores have lower melting points. The melting process for the solid is initiated from existing molten phase, such as the liquid-like layer that is retained at the pore wall even when that in the centre of the pore is frozen. In cylindrical pores, melting would occur at a lower temperature via a hemispherical meniscus (between solid and molten phases), than it would via a sleeve-shaped meniscus. By using scanning curves and loops, Hitchcock *et al*. [15] have recently shown that cryoporometry melting curves are prone to a pore-pore cooperative effect analogous to advanced condensation in gas adsorption. For a through cylindrical pore, melting is initiated, in a radial direction, from the thin cylindrical sleeve of permanently unfrozen liquid-like fluid that exists at the pore wall. However, if a small radius cylindrical pore is attached to a larger radius cylindrical pore at one end, in a funnel-like arrangement, then, once the smaller pore melts via its cylindrical sleeve meniscus, a hemispherical meniscus will be formed at one end of the larger pore. If the larger pore radius is smaller than the critical size for melting via a hemispherical meniscus at the current temperature, then the larger pore will also melt at the same temperature as the smaller pore. Hitchcock *et al*. [15] have shown that such advanced melting effects can lead to a dramatic skew towards smaller pores in PSDs for mesoporous sol-gel silicas, determined from cryoporometry melting curves.

Since PSDs are critical descriptors used to aid the understanding of the performance, and design, of porous heterogeneous catalysts, it is important to know their limitations. Studies of cooperative effects within model porous solids with controlled pore size and geometry, achieved either by templating (such as SBA-15 or MCM-48) or electrochemically-etching (such as alumina or silicon membranes), is of limited value in understanding the extent of the cooperative effects in more commonly used catalyst support materials, such as γ-alumina or sol-gel silica pellets, because of the limited size, and reduced complexity, of the controlled unit cell within the model materials. The only way to establish the extent and importance of the cooperative effects, particularly those of longer range, within amorphous materials is to study them directly. Hence, it is necessary to be able to isolate the individual stages in the

inception, growth and pervasion of cooperative processes within complex pore networks using highly sophisticated characterisation techniques. Therefore, in this work, it is proposed to study the progressive adsorption of water vapour within a mesoporous sol-gel silica using NMR cryoporometry, NMR relaxometry and NMR diffusometry at different relative pressures. Further, the particular material selected for this study possesses highly pronounced, macroscopic correlations in the spatial distribution of pore size, which makes it appropriate for studies of long-range effects, well beyond the unit-cell size of templated or etched model materials.

The filling of mesoporous silica materials with water has been studied previously using the three aforementioned NMR techniques, but, usually, only using each technique individually, or in concert with just one other method, and not using all three simultaneously. In early work, Allen *et al.* [16] studied the filling processes of water and cyclohexane in porous silica using NMR relaxometry and cryoporometry, and interpreted their data in terms of a 'puddle pore-filling model', whereby condensed liquid initially collects in particular concavities within the void space. These authors only considered growth in puddle size and geometry, and not the manner of that growth. More recently, Troyer *et al.* [17] have interpreted similar datasets in terms of a so-called 'plug model' of pore-filling. Farrher *et al.* [18] have used MRI without pre-conditioning and magnetization grid rotating frame imaging (MAGROFI) to study the spatial distribution of liquid within partially saturated silica samples. Their MRI studies demonstrated a heterogeneous spatial distribution of liquid on macroscopic length-scales. Naumov *et al.* [19] have studied the spatial arrangement of condensate within the void space, on the adsorption and desorption branches of the hysteresis loop region of the isotherm, for cyclohexane sorption in Vycor porous glass. They found that the diffusivity differed between the boundary adsorption and desorption branches of the hysteresis loop at the same degree of pore-filling. In addition they also found that the spatial arrangement of condensate at the same saturation level differed for scanning loops, when compared with the boundary curves. These results suggested that the spatial arrangement of condensate within pores was dependent upon the adsorption-desorption history of the sample.

In the work presented here, all three aforementioned NMR techniques will be used to study each stage in the progressive equilibrium adsorption of water vapour within a mesoporous silica, with an explicit aim to detect and study advanced adsorption, and melting, phenomena. In particular, the nature of the pore-filling process will be followed to determine how and when the advanced phenomena arise. In addition, cryoporometry scanning loops will be used to assess the reversibility of the melting process, and the connectivity of the condensed phase following adsorption to different relative pressures.

THEORY

NMR diffusometry

Pulsed field gradient (PFG) NMR can be used to determine the effective diffusion coefficient of a molecule within a sample. The reduction in signal intensity with increasing gradient strength is related to the observed diffusion coefficient according to the relationship derived by Wu *et al.* [20]:

$$I = I_0 \exp\left(- D\gamma^2\delta^2 g^2 \left(\Delta - \frac{\delta}{3} - \frac{\tau}{2} \right) \right), \qquad (1)$$

where I_0 is the signal intensity with no field gradient applied, D is the observed diffusion coefficient, γ is the gyromagnetic ratio, δ is the length of the applied field gradient, g is the field gradient strength, Δ is the diffusion time, and τ is the correlation time between bipolar gradients.

In the experiments considered in this work, diffusion is occurring within the molten, adsorbed ganglia of water, as any bulk water will be frozen. Adsorbed ganglia may be complex in

geometry and topology, and extend beyond a single pore. At the very shortest diffusion times, the diffusing molecule is free to explore the localised ganglia topology, and will henceforth be referred to as unrestricted diffusion (though, of course, it will still be confined due to local pore walls and menisci). At slightly longer diffusion times, the motion of the molecule within each ganglion may become restricted by collision with the outer, boundary perimeter (i.e. edge) of the ganglion formed by the vapour-liquid meniscus and/or solid walls of the pore, and, therefore, the measured effective diffusion coefficient is indicative of the overall 'cavity size' of the confining ganglion. At the longest diffusion times, if the ganglia are all isolated, all molecular motion will become completely restricted, or, if the ganglia are interconnected, the molecule may find (a potentially narrow exit and) leave the cavity formed by the proximity of various nearby pore walls and menisci, and begin to probe the wider interconnected ganglia network, and then the measured diffusion coefficient is indicative of the overall tortuosity of the continuous, adsorbed phase. In between these limits, it is likely that there will be a combination of restricted and unrestricted diffusion.

For diffusion within the adsorbed phase, the tortuosity of the ganglia network may be obtained using the expression [21]

$$\tau_p = \frac{D_b}{D_{eff}}, \qquad (2)$$

where τ_p is the apparent tortuosity of the liquid ganglion, D_b is the bulk, free diffusion coefficient at the appropriate temperature, and D_{eff} is the observed or effective diffusion coefficient. Faster diffusion is associated with a smaller value of tortuosity, while slower diffusion is associated with high tortuosity.

In this work, the self-diffusion of molten phase (water) will be studied within the ganglia of adsorbed phase. The root mean square (rms) displacements of the water molecules during the PFG NMR experiments will typically be smaller than the overall spatial extent of particular

ganglia, but diffusion times will be employed such that a fraction of diffusing molecules will sense the outer perimeter at the edge of a ganglion. Hence, following the suggestion of Gjerdåker *et al.* [22], the short time diffusion model of Mitra *et al.* [23] will be applied to the PFG NMR data, and extrapolation made to zero observation time to obtain an unrestricted diffusivity within the local liquid ganglion. Mitra *et al* [23] have shown that a perturbation expansion of the measured diffusivity will deviate from the macroscopically unrestricted intra-ganglion diffusion coefficient D_0, given by the following equation:

$$D(\Delta) = D_0 - \frac{4D_0^{3/2}S}{9\pi^{1/2}V}\Delta^{1/2}, \qquad (3)$$

where S is the external surface area of the perimeter of the ganglion region, and V is the volume contained within the perimeter of the ganglion region. A straight line fit of PFG NMR data for measured diffusivity (or reciprocal tortuosity) against $\Delta^{1/2}$ should thus yield an intercept equal to the unrestricted matrix diffusion coefficient D_0 (or $1/\tau_0$).

NMR relaxometry

NMR relaxometry will be used to probe adsorbed ganglia sizes. The intensity of the transverse magnetisation in NMR, I, decays, from an initial value of I_0, with a time constant known as the spin– spin relaxation time, denoted T_2, according to the expression.

$$I = I_0 \exp(-t / T_2) \qquad (4)$$

where t is the time. For more heterogeneous samples a two-component relaxation model was used:

$$I = I_0 [a \exp(-t / T^f_2) + (1-a) \exp(-t / T^S_2)] \qquad (5)$$

where T^f_2 and T^S_2 are the relaxation times for the fast and slow components, with fractions a and $(1-a)$, respectively.

The value of T_2 may be converted to a surface area to volume ratio by the adoption of a relaxation model. For a liquid imbibed within a confined space, the relaxation rate is enhanced. This is due to the particular thin layer of liquid in close proximity to an interface being affected by its presence, thereby increasing the relaxation rate. There is also diffusional exchange between the surface-affected layer and the remainder (bulk) of the liquid. In the case, as here, where the liquid ganglia are several orders of magnitude smaller than the rms displacement of the probe water molecules during the course of the experiment, the‘‘two-fraction fast exchange model’’ of Brownstein and Tarr [24] can be used. The measured value of T_2 is given by

$$\frac{1}{T_2} = (1 - \lambda S_v)\frac{1}{T_{2B}} + \lambda S_V \frac{1}{T_{2S}} \ , \qquad (6)$$

where the T_{2S} and T_{2B} refer to the relaxation on the surface layer and bulk fluid, respectively, λ is the thickness of the surface-affected layer, and S_V is the surface area to volume ratio. In general $T_{2B} >> T_{2S}$ and thus S_V is given, approximately, by:

$$S_v = \frac{T_{2S}}{\lambda}\frac{1}{T_2} . \qquad (7)$$

For example, for a completely saturated cylindrical pore, S_V would be equal to $2/r$, where r is the radius. Therefore, T_2 is then proportional to the pore size.

EXPERIMENTAL

The material studied in this work was a batch of commercially-available sol-gel silica spheres, denoted S1, of diameter ~2-3 mm. The batch average BET specific surface area is ~200 m^2g^{-1}, and the batch average specific pore volume estimated from the sample studied in this work is ~0.80-0.92 cm^3g^{-1}, but there are some differences between individual pellets due to intra-batch variability. This material has been extensively characterised in our earlier work, including pore size distributions obtained from gas sorption, mercury porosimetry and NMR cryoporometry [15,25]. We have also applied our novel integrated gas sorption and

mercury porosimetry technique to this material [25]. Sodium hydroxide (NaOH) (99.99% trace metals basis) was purchased from Fluka. Prior to the adsorption experiments, the samples were pre-soaked in ultra pure water, and then the bulk and physisorbed moisture was removed by degassing for 2 hours at 90 ^{o}C, followed by 10 hours at 120 ^{o}C. These conditions were chosen to avoid any partial dehydroxylation of the silica surface, since only water physisorption is required.

Water adsorption

In order to obtain relative pressures of water vapour of 0.81-1.0 (capillary condensation region), the sol-gel pellets were suspended above NaOH solutions of different concentrations [26]. The samples were then left to equilibrate for 5-7 days at 294 K, over a 'large' solution reservoir, in order to permit the assumption that the concentration of NaOH remains constant throughout the adsorption process. The points of the water isotherm were obtained by gravimetrically measuring the water uptake of thirty similarly sized pellets, at each relative pressure.

For the NMR experiments, a given sample, consisting of a single pellet, was prepared identically to as described above, and then was quickly transferred to an NMR tube. The experimental set-up and procedures were as described below. Single pellet samples were weighed before and after experiments to check that no significant liquid evaporation occurred during the course of transfer to the NMR tube etc. Sets of cryoporometry experiments were performed at different saturation levels for the same single pellet sample. For the NMR experiments, two different single pellet samples from the same batch were used. Sample 1 was used to generate cryoporometry melting curves, and T_2 and tortuosity values for fully molten samples at each relative pressure in the range between 0.81-0.94. Sample 2 was used to generate boundary melting curves, scanning loops, and T_2 and tortuosity values for both the fully and partially molten sample, after equilibration with water vapour at relative pressures of 0.92 and 1.0.

NMR cryoporometry

All NMR experiments were carried out on a Bruker Avance 400 MHz spectrometer with a static field strength of 9.4 T, yielding a resonance frequency of 400.13 MHz for ^{1}H nucleus. The temperature control unit within the probe uses a controlled flow of cool nitrogen gas evolved from liquid nitrogen, in combination with a heating element below the sample in the gas flow stream. Temperature control was achieved using a Bruker BVT3200 temperature control unit, able to measure and maintain the probe temperature within ±0.1 K within the range of 123–423 K. The chosen pulse sequence was a simple spin-echo sequence, a more basic form of the Carr–Purcell Meiboom–Gill (CPMG) sequence [27]. The choice of the simple spin echo pulse sequence was made according to literature [28-30] as it accounts for small magnetic field inhomogeneities that are present within the sample, therefore enhancing the quality of the signal obtained. A CPMG sequence was not used due to the hardware limitation not permitting the delay time between the successive 180° pulses to be less than 1.2 ms, while the echo time has to be kept at 2 ms to suppress the signal from the liquid like layer. The echo time (2τ) was 2 ms to compensate for the liquid like layer relaxation on the pore surface.

A single saturated pellet was placed within a 5 mm NMR tube, between two susceptibility plugs to reduce the water evaporation from the pores. A thermocouple was used to measure the real temperature of the sample and it was placed on to the top of the pellet, via a hole in the centre of the top susceptibility plug. The sample was frozen down to 240 K, and then the temperature was increased stepwise. At each step, it was then allowed 15 min to reach equilibrium and a series of proton spin-echo spectra was taken for each saturation, at each temperature. This time proved to be sufficient for the system to complete any phase transition at each temperature change. All the molten fractions are normalized to the 100 % molten fraction at the top of the pellet melting curve for the 100% saturated sample (at $P/P_0=1$). It was noticed that, for samples below $P/P_0=0.81$, the FID was inadequate; hence all the samples used for the cryoporometry experiments, were saturated at higher relative pressures. As there is no bulk liquid on the surface of the pellet, the total FID at ~273 K corresponds only to total water adsorbed within the pores. Application of a suitable correction of the results for the Curie law was found to make no significant difference.

NMR relaxometry

For the relaxometry experiments, the samples were prepared as described above and T_2 relaxation was measured, using a CPMG sequence. For Sample 1 of S1, relaxation time measurements were performed at the 100% molten fraction, for each relative pressure, at ~273 K. For Sample 2, relaxation time measurements were obtained at various positions around the scanning loops, as detailed in Table 1. The time between 180° pulses in the CPMG sequence, for all relaxation experiments, was 1.2 ms. It was found that the single component model (eq 4) gave a good fit to data for fully molten samples, while the greater heterogeneity of the partially molten samples required a fit to the two-component relaxation model (eq 5).

NMR diffusometry

All PFG-NMR experiments were carried out using the NMR system described above. The pulse sequence used was a stimulated echo with bipolar longitudinal eddy current delay (BPLED) developed by Wu *et al*. [20]. The values of δ and τ were 0.002 and 0.0001 s, respectively, and the diffusion times, Δ, used, were 0.05, 0.1, 0.15 and 0.2 s. For each diffusion experiment, 10 data points were taken at increasing gradient strengths between 0.674 and 33.143 G cm^{-1}, and each point was obtained with 16 scans.

The apparent diffusion coefficients were measured at ~273 K, corresponding to the completely molten state for Samples 1 and 2, and at 270.6 K for the partially molten state of Sample 2 when fully saturated, and were calculated from the signal attenuation observed during the experiment. To account for any temperature dependency of the apparent diffusion coefficient between the experiments, a calibration curve of bulk water was used based upon literature data [31]. The tortuosity values were then calculated using eq. 2.

RESULTS

Water adsorption

Figure 1(a) shows the equilibrium water sorption isotherms obtained gravimetrically for a sample of 30 pellets from batch S1 used in this work. The shape of the hysteresis loop is Type H2, which is similar to that generally obtained for nitrogen adsorption in disordered, mesoporous solids [1]. For comparison purposes, also shown in Figure 1(b) is the water adsorption isotherm obtained by NMR for the particular pellet sample used to obtain the data given in Figure 2 (Sample 1). While the isotherms shown in Figures 1(a) and (b) are very similar, the slight differences result from the intra-batch variability between individual pellets from the same batch, sometimes found in commercial materials. Hence, a given single pellet may behave differently from the batch average result shown by the gravimetric isotherm.

(a)

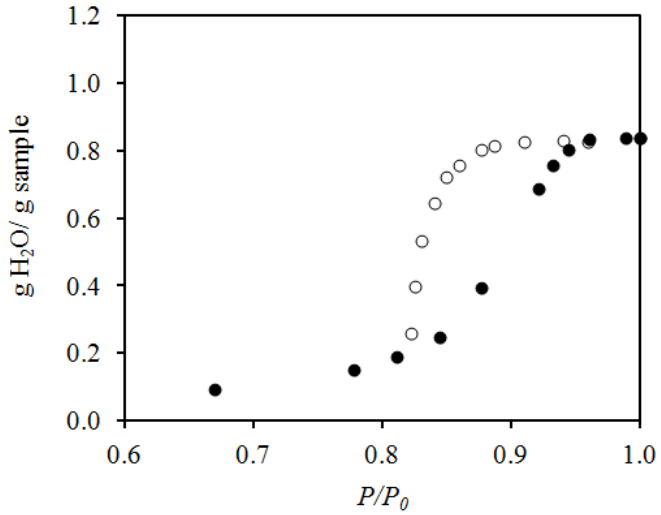

(b)

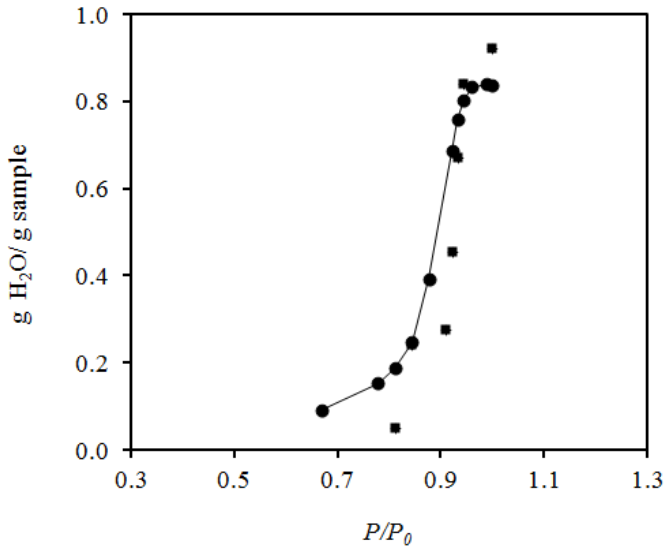

Figure 1.

(a) Normalized water adsorption (●) and desorption (o) isotherms for a sample of 30 pellets from batch S1, obtained at 294 K. The water uptake was measured gravimetrically. (b) Comparison of adsorption isotherm obtained gravimetrically for 30 pellets (●) with that obtained by NMR for one pellet (■) of Sample 1. The line shown is to guide the eye.

NMR cryoporometry

Figure 2(a) shows the melting curves obtained for the adsorbed phase within a single pellet sample, denoted Sample 1, at various different relative pressures of water vapour in the range 0.81-0.94. The molten volume fractions, at different relative pressures, are measured relative to the total pore volume of this pellet, and, thus, the ultimate molten volume fractions achieved for experiments below total saturation are less than unity. From Figure 2(a), it can be seen that, with increasing relative pressure, the melting curves move to higher temperatures and the steps up in intensity become more abrupt (i.e. spread over a smaller temperature range). In particular, it is noted that the melting curves for relative pressures of 0.91 and 0.92 generally overlay each other up to ~269.5 K, after which they diverge. The 0.92 relative pressure curve rises more abruptly than that for the 0.91 relative pressure curve, as highlighted in the inset in Figure 2(a). However, it is noted that the 0.91 relative pressure curve shows a significantly larger increase in signal intensity over the higher temperature range ~270.3-270.7 K than 0.92 relative pressure curve, despite the larger overall final intensity of the latter.

Using the Gibbs-Thomson equation [13], the apparent PSDs were obtained from the melting curves for Sample 1. Cryoporometry is an indirect pore size characterisation technique, since, to obtain absolute pore sizes, requires a calibration of the Gibbs-Thompson parameter against pore size measures from another technique. Hence, we have, thus, used a reduced pore size (r/r_{ref}), with the point of inflexion in the relevant melting curve taken as the reference size, r_{ref}, that is taken to correspond to the equivalent inflexion point from the cumulative PSD derived from nitrogen adsorption. The PSDs from the melting curves were compared with that obtained from nitrogen adsorption using the BJH algorithm, and the results are shown in Figure 2(b). From Figure 2(b), it can be seen that the cryoporometry PSD of the partially saturated sample (P/P_0 = 0.91) is wider than that for the fully saturated sample. A comparison of the PSD obtained from cryoporometry for a fully saturated sample, and that from gas adsorption, shows clearly that cryoporometry underestimates the width of the PSD, and, thus, that advanced melting and advanced adsorption are not completely analogous in complex materials.

(a)

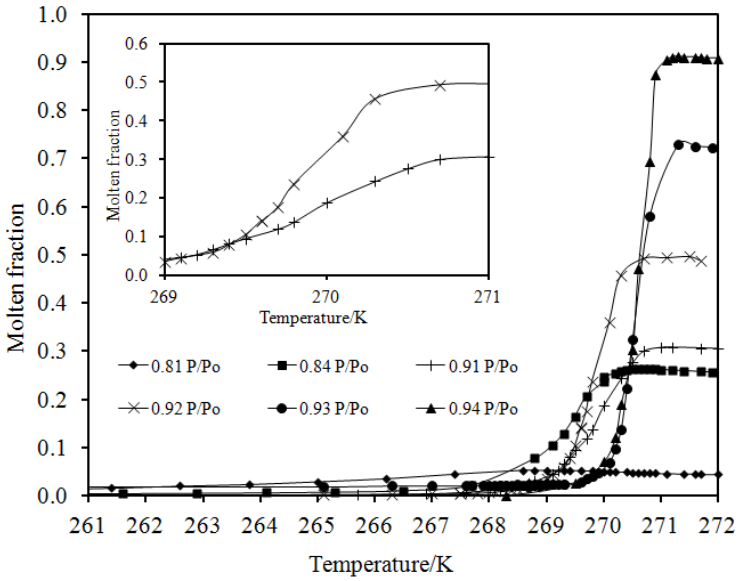

(b)

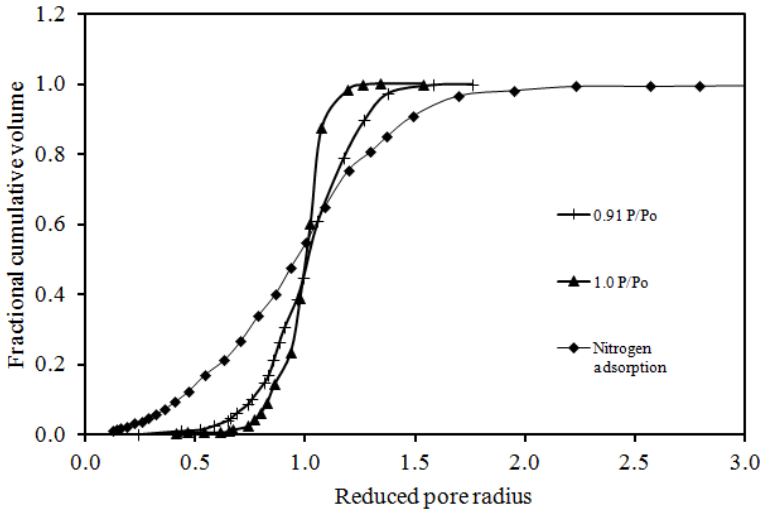

Figure 2.

(a) NMR cryoporometry melting curves for the adsorbed phase in a single pellet sample of S1 (Sample 1) at different relative pressures of water vapour. The inset shows a close-up view of the steep parts of the melting curves for relative pressures of 0.91 and 0.92. The lines shown are to guide the eye. (b) PSDs derived from the melting curve in (a) for a relative pressure of 0.91, and the melting curve for a relative pressure of 1.0, and, also, the PSD derived from nitrogen adsorption using the BJH algorithm.

Figure 3 shows the boundary melting curves, and a set of scanning loops, for another single pellet sample from batch S1, denoted Sample 2, following equilibration with water vapour at relative pressures of 0.92 and 1.0. For both saturation levels, the scanning loops have the same starting point, which is with ~51% of the total pore volume in the molten state. For the sample equilibrated at a relative pressure of unity, two scanning loops are shown, namely one which ends at the same temperature as the loop for the sample equilibrated at a relative pressure of 0.92 (wide loop), and one ending at the same molten fraction as the loop for the sample equilibrated at a relative pressure of 0.92 (small loop). From Figure 3 it can be seen that the boundary melting curve, for the sample equilibrated at a relative pressure of 1.0, begins to rise at a significantly lower temperature, and rises more steeply, than that for the sample equilibrated at relative pressure of 0.92. It is also noted that, while the freezing (upper) arm of the scanning loops for the sample equilibrated at a relative pressure of 1.0 more or less overlay the upper arm of the scanning loop for the sample equilibrated at a relative pressure of 0.92 for the range of temperatures ~270.5-269.5 K, they drop below it at lower temperatures. Hence, a larger volume of pores is frozen over the same drop in temperature for the sample equilibrated at a higher relative pressure.

From Figure 3, it can be seen that the melting arms of the scanning loops for the sample equilibrated at a relative pressure of 1.0 begin to rise at a lower temperature than the corresponding boundary melting curve. However, an early rise is not so evident in the melting arm of the scanning loop for the sample equilibrated at a relative pressure of 0.92, where the lower temperature section is much flatter.

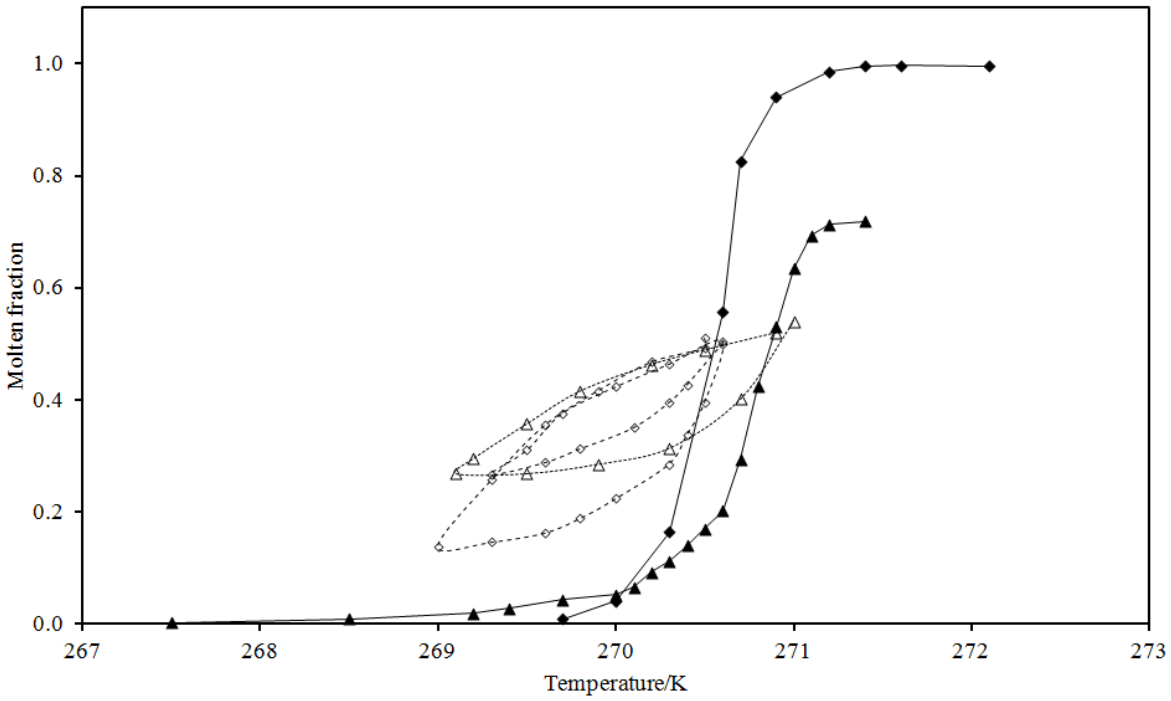

Figure 3

NMR boundary (solid symbols) freezing and melting curves, and scanning loops (open symbols), obtained for a single pellet sample of S1 (Sample 2) at two different relative pressures (0.92 (triangles) and 1.0 (diamonds)) of water vapour. The lines shown are to guide the eye.

NMR relaxometry

Figure 4 shows the variation in T_2 of the adsorbed phase with relative pressure (humidity) for the same pellet sample as used to obtain the data in Figure 2(a) (Sample 1). It can be seen that after an initial rise up to a relative pressure of 0.84, the T_2 value stays roughly constant until a relative pressure of 0.92, when it begins to rise steeply. All of the data from the relaxation experiments for fully molten samples exhibited mono-exponential log-attenuation behaviour, suggesting that extensive diffusional averaging of the size of the liquid ganglia, arising at each pressure, was occurring. Figure A1 (Appendix) shows an example of the log-attenuation plot, fitted to the raw relaxation data, obtained for Sample 1 at low saturation (relative pressure 0.84).

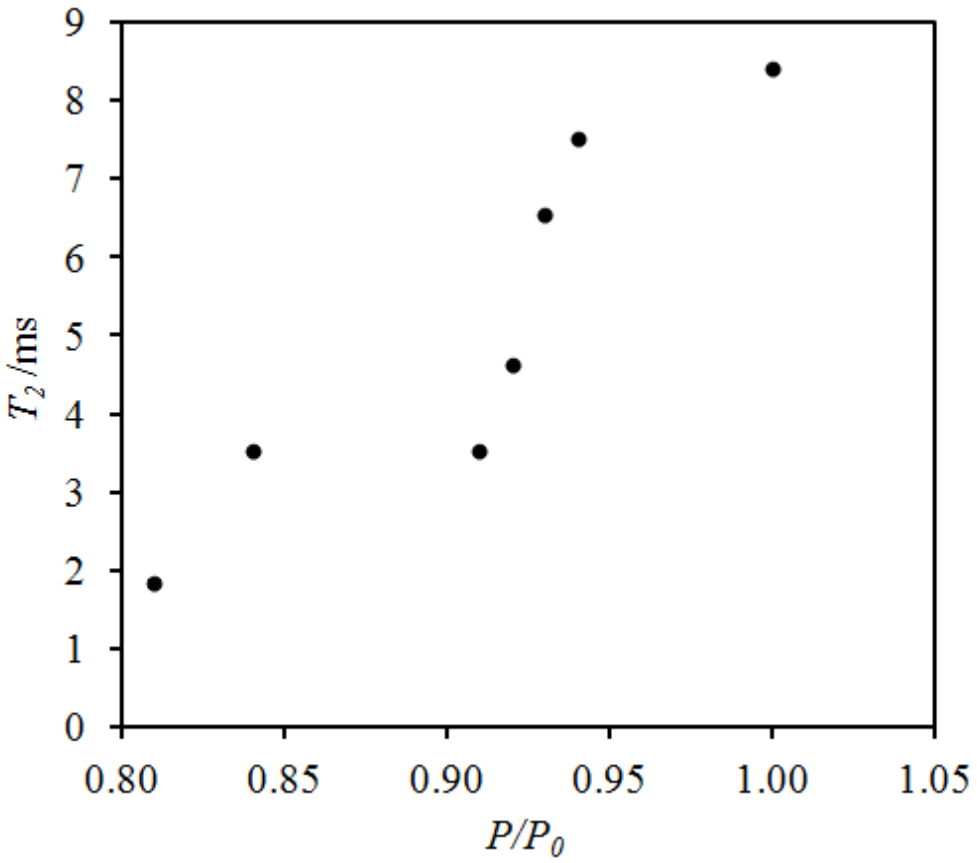

Figure 4.

Variation of NMR spin-spin relaxation time (T_2) for the adsorbed phase, obtained at the top of the melting curves (all at 273 K), with relative pressure (P/P_0) of water vapour for the sample of S1 used to obtain the data in Figure 2 (Sample 1). The errors in the T_2 values are smaller than the size of the symbols.

Studies of the variation in T_2 values with temperature, along the flat plateau at the top of the boundary freezing curve for a fully saturated sample, suggest that there is insignificant temperature dependence of T_2 values (±0.12 s maximum error) over the narrow temperature range of interest between the boundary curves. Table 1 shows the results of fitting a two-component relaxation time model to the relaxometry data obtained at different positions around the scanning loops for Sample 2, shown in Figure 3. Table 2 shows the T_2 values obtained for the upper regions of the boundary melting curves for Sample 2. From Tables 1

and 2, it can be seen that, while the T_2 value at the top of the scanning loop, for the sample equilibrated at 0.92 relative pressure, is higher than that at the top of the scanning loop for the sample equilibrated at 1.0 relative pressure, when the molten fraction increases to 0.72, the T_2 value for the sample equilibrated at 0.92 relative pressure becomes higher than that at the top of the scanning loop for the sample equilibrated at 1.0 relative pressure, despite still corresponding to a lower melting temperature. Further, it is noted that the T_2 value at the bottom of the scanning loop, for the sample equilibrated at 0.92 relative pressure, is higher than that corresponding to the same temperature (within experimental error) at the bottom of the scanning loop for the sample equilibrated at a relative pressure of 1.0.

NMR diffusometry

Raw log-attenuation data was obtained for diffusion within the molten phase at the top of the melting curve (where any bulk liquid in the thin external film would still have been frozen if any had existed) for Sample 1. These data were fitted to a single exponential model according to eq 1, and found to give rise to good fits. Since a single-component model gave a good fit to the raw log-attenuation data, this is consistent with the gas phase not making a significant contribution to mass transport, because, otherwise, a second, fast diffusing component might be anticipated. For each relative humidity, the set of values of diffusivity thus obtained, at different diffusion times, were then fitted to the model for partially restricted diffusion as given by eq 3. These data all gave rise to good fits to the partially-restricted diffusion model. The limiting values of the apparent tortuosity for unrestricted (but confined) diffusion were then obtained using the value of bulk (free) diffusivity appropriate to the relevant temperature. The rms displacements calculated from the unrestricted diffusivity are consistent with liquid-phase only mass transport, as there was no indication of diffusion apparently occurring faster than for bulk liquid. Figure 5 shows the variation of unrestricted diffusion tortuosity with relative humidity (pressure) for the same pellet sample as used to obtain the data in Figure 2(a) (Sample 1). It can be seen that the tortuosity is roughly constant until a relative pressure of 0.91, and thereafter it declines rapidly with increasing relative pressure.

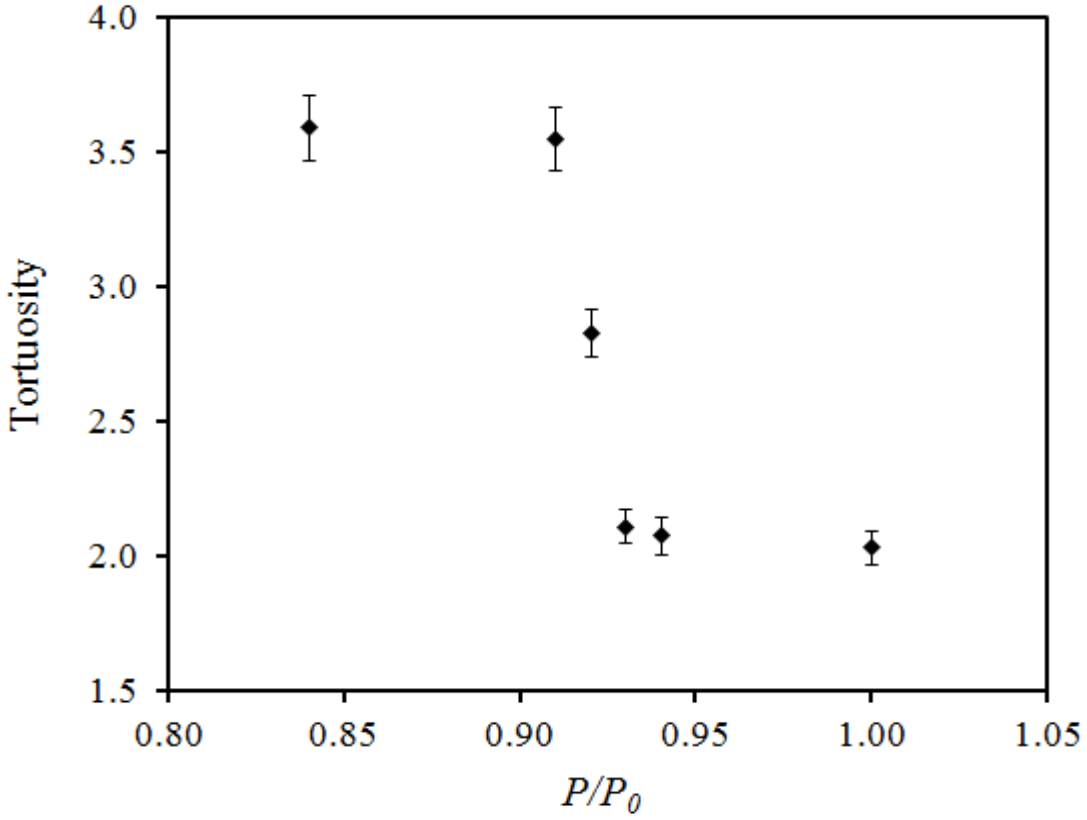

Figure 5.

Variation of unrestricted diffusion tortuosity for the adsorbed phase, obtained at the top of the melting curves (all at 273 K), with relative pressure (P/P_0) of water vapour for the sample of S1 used to obtain the data in Figure 2 (Sample 1).

During the PFG experiments, it is likely that there was negligible exchange between the vapour and liquid phases within the pores, even at the very low saturation levels where a larger fraction of the void space was occupied by vapour. This is because, as shown in the typical data-set for a sample saturated at relative pressure of 0.84 given in Figure A2 (Appendix), a mono-exponential fit (eq. 1) to the log-attenuation data was found to be sufficient, which would have been unlikely if significant exchange was occurring between two different phases.

Table 2 shows the values of tortuosity obtained from PFG NMR experiments conducted on Sample 2 when fully molten following equilibration at a relative pressure of 0.92 and 1.0, and when partially molten (on the boundary molten curve), following equilibration at a relative pressure of 1.0, where the overall molten volume is the same as when fully molten following equilibration at a relative pressure of 0.92. It can be seen that the tortuosity is higher for the sample with the lower saturation level when it is fully molten, compared with the partially molten, fully saturated sample at the same (or higher) molten fraction.

DISCUSSION

Advanced melting occurs when the molten phase occupying a small pore immediately adjoins the frozen phase in a larger pore. The effect is thus facilitated by increased inter-connectivity of the occupied void space, since then more pores would have increased numbers of neighbours also filled with condensate that might potentially aid their own melting. Hence, a pore network with a lower pore connectivity will have less potential connections via which advanced melting could occur. Steadily increasing the liquid saturation level towards complete pore-filling will progressively fill pores within the network, thereby also progressively improving the level of pore interconnections within the network. Hence, it would be expected that the opportunities for advanced melting would increase with increased pore-filling. This procedure also allows the study of the importance of the various individual pores to the overall connectivity of the network in the fully saturated state. If a critical pore becomes filled at a given relative pressure then the connectivity will rise significantly. In a fully saturated sample, it is these critical pores that will also permit the rapid transmission of the advancing meniscus as the melting front percolates the network following a temperature increase. Hence, the study of the partially saturated samples allows the identification of these critical pore sizes that greatly impact the advanced melting process in the fully saturated sample. It is these critical pore sizes that would feature prominently in a cryoporometry PSD.

The PFG NMR data for Sample 1 suggests that there is a relatively rapid decline in tortuosity of the adsorbed phase between relative pressures of 0.91-0.92. Decreasing tortuosity is associated with increased inter-connectivity of the diffusing phase, since it facilitates easier diffusion. Hence, the PFG NMR data suggests that the large increase in the adsorbed phase inter-connectivity, which would be necessary to facilitate advanced melting, did occur when the melting curves indicated that the influence of advanced melting had increased. The abrupt increase in phase connectivity, observed after a relative pressure of 0.91, is akin to the similar sharp transition generally observed during the formation of the sample-spanning cluster at the onset of percolation of the vapour phase during gas desorption. For Sample 2, the tortuosity for the fully molten sample was 2.25±0.07 and 1.82±0.05, when the sample had been equilibrated at water relative pressures of 0.92 and 1.0, respectively. Higher tortuosities are generally associated with lower connectivities. Hence, the interconnectivity of the adsorbed phase is probably higher at higher relative pressure, as might be expected. A higher inter-connectivity of condensed phase at a relative pressure of 1.0 is also consistent with the differences observed in the form of the scanning loops when Sample 2 had been equilibrated at relative pressure of 1.0, compared with a relative pressure of 0.92. A higher connectivity of the condensed phase would better facilitate initiation of advanced melting, from the molten remnant, on the melting arm. Higher interconnectivity would also lead to less shielding during invasion percolation of the freezing front, and thus more pores freezing, on the freezing arm of the scanning loops. The higher T_2 value at the lower temperature end of the freezing arm of the 0.92 relative pressure loop, compared with the equivalent location for the relative pressure of 1.0 loop ending at the same temperature, suggested that some larger pores remain shielded in the former, despite the same neck sizes potentially being frozen.

The melting curve data for Sample 1 for the relative pressures of 0.91 and 0.92 are consistent with the onset, between these relative pressures, of significant advanced melting at the point where they diverge (~269.5 K). The steeper shape of the upper part of the melting curve for 0.91 relative pressure, compared with that for a relative pressure of 0.92, suggests that the larger pores, melting between ~270.3-270.7 K, occupied by condensate at the lower pressure, are, apparently, no longer occupied at the higher pressure. The range of this discrepancy greatly exceeds the size of the estimated, potential error in the temperature measurement of 0.1 K. Since this lack of occupation at higher pressure seems unlikely (as higher pressures

tend to increase occupancy of larger pores by condensate, not reduce it), the alternative interpretation is that the steep deviation upwards, at ~269.5 K, in the melting curve for the 0.92 relative pressure, from that for 0.91 relative pressure, represents the onset of a significant advanced melting effect. This would mean that pores melting at a lower temperature than ~270.3 K, for data for a relative pressure of 0.92, have also facilitated the lower temperature melting of those pores that originally melted between ~270.3-270.7 K for data for a relative pressure of 0.91. Since this effect only arose once the relative pressure had increased from 0.91 to 0.92, leading to an increase in ultimate fractional saturation from ~0.3 to ~0.5, this would suggest that some of the pores filling between those pressures enabled the advanced melting to occur.

For Sample 2, the melting curves for relative pressures 0.92 and 1.0 bear a similar relationship to each other, in terms of overall form and relative position, as the melting curves for relative pressures of 0.91 and 0.92 do for Sample 1. In each case, the higher relative pressure melting curve deviates from the lower relative pressure curve at a low molten fraction, and then rises steeply on the lower temperature side of the lower relative pressure curve. For Sample 2, the change in molten fraction in the range 270.7-271.2 K is much less for the higher relative pressure curve. As with the analogous result for Sample 1, this discrepancy has arisen because advanced melting has meant that some of the pores that previously melted in this higher temperature range, at lower relative pressure, have, at higher relative pressure, melted at lower temperatures despite their large size. There was an increase in the T_2 values, occurring between molten fractions of 0.51 and 0.72 on the boundary melting curve obtained at relative pressure of unity, to beyond the T_2 value for a molten fraction of 0.51 on the 0.92 relative pressure curve. This increase in the T_2 values, occurring despite the corresponding melting temperature not also, concomitantly, increasing beyond that point for the 0.92 relative pressure curve, suggested significant advanced melting was occurring on the relative pressure of unity curve between molten fractions of 0.51 and 0.72. The difference, between Sample 1 and Sample 2, in the relative pressure range over which boundary melting curves have a similar form must reflect differences in the spatial disposition of adsorbed phase, at the same relative pressure, between these samples. As mentioned above, a more interconnected adsorbed phase would better facilitate opportunities

for advanced melting. Hence, advanced melting effects are a definitive probe for the development of interconnectivity of adsorbed phase for a given sample.

These above findings enable an assessment to be made of which particular pores facilitate the advanced melting of which other pores, and thus the likely inaccuracies in the final cryoporometry PSD over a given pore size range. The pore size distribution for S1 can be determined from the melting curve using a value of 26 nm K for the group of physical constants in the relationship between melting point depression and pore core size [13]. This value was assumed since advanced melting occurs via a hemispherical meniscus. It was assumed that the thickness of the pore surface layer left as unfrozen liquid-like phase was 0.4 nm [32]. Using these parameters this would suggest that particular advanced melting identified for Sample 1 in Figure 2(a) above would mean that at least 37 % of the pores in the range 9.9-11.4 nm would be missed using NMR cryoporometry. This missing pore volume would be attributed to smaller pore sizes in the range 7.9-9.9 nm. For Sample 2, the advanced melting seen in Figure 3 would lead 26 % of the total pore volume that actually consists of pores in the size range 11.4-14.1 nm to be falsely attributed to pores in the size range 9.1-11.4 nm, if the boundary melting curve for the fully saturated sample were used to derive the PSD.

The cryoporometry, relaxometry and diffusometry data obtained here can also shed light on the pore-filling mechanism for S1 sol-gel silica. Previous work, using ^{1}H solid-state NMR, has suggested two different pore-filling mechanisms for water adsorption in silica-based materials [33, 34]. Pore-filling in SBA-15 and controlled pore glass (CPG) involved, after initial coverage of the surface, a radial growth in the surface film towards the pore axis [33, 34]. However, for MCM-41, the proposed mechanism involved initial wetting of the surface, then a coexistence of filled pores, or pore segments, with wetted pores, or pore segments, and then further filling occured as a growth of the filled pores involving an axial filling of the pores. Grünberg *et al.* [33] suggested that the observed difference in pore-filling mechanism arose because of the difference in pore sizes between SBA-15 and MCM-41. Further, as mentioned above, Troyer *et al.* [17] proposed an alternative, ‘plug-model’, pore-filling mechanism, for water adsorption in silicas, distinct from the puddle-growth model of Allen *et al.* [16]. Troyer *et al.* [17] suggested that adsorption began as an adsorbed film, that then

grew into undulates, that then met to form a plug of liquid bridging the pore cross-section completely. The pore then filled by axial growth of this plug. These workers then used relaxometry data to study pore-filling in CPG.

The data obtained for Sample 1 of S1 can be considered in the light of this previous work. The gradual shift to higher temperature in the melting curves up to relative pressures of 0.91 is consistent with a growth in the thickness of an adsorbed film, or the growth in size of adsorbed puddles. However, the steep increase in relaxation time of the adsorbed phase, between relative pressures of 0.91-0.92, would be consistent with the onset of the meeting and merger of adsorbed films, or undulates, from opposite sides of a pore. This is because, if this merger were to occur, the characteristic size of the adsorbed phase, governing relaxation rate, would then jump from the film, or undulate, thickness, to the diameter of the pore, since the liquid molecules would suddenly then be able to traverse the pore diametrically, through a large zone of bulk-like phase, rather than around the walls in closer proximity to the surface-affected layer. This change in freedom of motion might also be partly associated with the above observed decrease in the tortuosity of the adsorbed phase, as well as that originating from increased connectivity due to increased saturation. Once formed, the adsorbate plug could fill the pore radially, thereby giving rise to the hemispherical menisci that facilitate advanced melting and advanced adsorption.

However, the difference, in the variation in the shape and position of the melting curves between relative pressures of 0.92 and 1.0, observed for Samples 1 and 2 suggests a difference in the pore-filling process between the two samples for the respective critical pores governing advanced melting. The shift higher in temperature of the ‘lift-off’ point (where the gradient increases steeply) of the melting curves for Sample 1, between relative pressures of 0.92 and 0.93, suggests that the critical neck of condensed phase that initiates melting at 0.92 probably only occupies part of a pore cross-section. The shift in the position of the lift-off point is thus associated with the complete-filling by 0.93, and thus a larger ice crystal size, for the critical pore. The subsequent changes in the shape of the melting curve for Sample 1, between relative pressures of 0.93 and 0.94, just represent the filling of more larger (than the existing critical neck size) pores connected to the original cluster of filled pores present at

relative pressure of 0.93. However, for Sample 2, previously empty critical necks completely fill between a relative pressure of 0.92 and 1.0, leading to a large interconnected condensate network, and thus there is a shift in only the body of the boundary melting curve (and not the base) with increased relative pressure, and that shift is towards lower temperature.

As the results shown in Figure 2(b) indicate, in general, advanced melting is more acute than advanced adsorption for the S1 material. However, the above data can also be used to gain insight into advanced adsorption processes. If adsorption was occurring without advanced adsorption and pores simply filled in order of increasing size, the melting curves for successive relative pressures would be expected to show the form seen for the boundary melting curves obtained at relative pressures of 0.93 and 0.94 for Sample 1. As the relative pressure is increased, without advanced adsorption, only larger pores fill with condensate, and, thus, the melting curve for the higher relative pressure then only deviates from the curve obtained at lower relative pressure towards the top of that curve, thereby simply reflecting the melting of the additional larger pores at higher temperature. However, if some smaller pores fill with condensate only at higher relative pressure than some larger pores, then there is the potential that the newly-filled smaller pores can act as a nucleation site for advanced melting that did not exist previously (at lower pressure). In that situation, the melting curve obtained at higher relative pressure would be expected to deviate from that obtained at lower relative pressure towards the lower end (at lower molten fraction) of that curve (in contrast to the scenario above without advanced adsorption), where the critical new small pore melts, and rise more steeply (over a narrower, and lower, temperature range) than that lower relative pressure melting curve. This is what has been observed for the boundary melting curves obtained for Sample 2 equilibrated at relative pressures of 0.92 and 1.0. Hence, this suggests that the larger pores, melting at temperatures ~271 K in the melting curve for a relative pressure of 0.92, fill at a lower pressure than the smaller pore that melts at ~270.2 K, in the curve obtained at relative pressure of 1.0, that represents the critical size where the steep rise of the higher pressure melting curve starts.

Accurate pore size distributions are essential if they are to be used successfully in understanding phenomena such as relative catalyst activities. The above findings suggest that

pore-size distributions obtained using the typical experimental methods (employing boundary curves alone, for whole samples), and usual analysis techniques, are likely to be inaccurate in the presence of advanced phenomena. As shown above, these phenomena can be detected using additional cryoporometry experiments run on partially saturated samples. Hence, it is recommended that these experiments are run in addition to the standard experiment. Alternatively, for those materials, such as S1 [35], that are known, or suspected, to have macroscopic heterogeneities in the spatial distribution of pore size, the presence of advanced phenomena can also be detected and removed (to some degree) by obtaining the pore size distribution for the fragmented sample, as shown for the cryoporometry data for sample S1 in Figure 6. Figure 6 shows the cryoporometry data, for a fully saturated void space, obtained before and after fragmentation of a sample of S1. It can be seen that the pore size distribution for the fragmented sample is much wider than that for the whole sample, which is what would be expected if (at least some of) the effects of advanced phenomena had been removed by fragmentation because regions of larger pores were no longer connected to those of smaller pores.

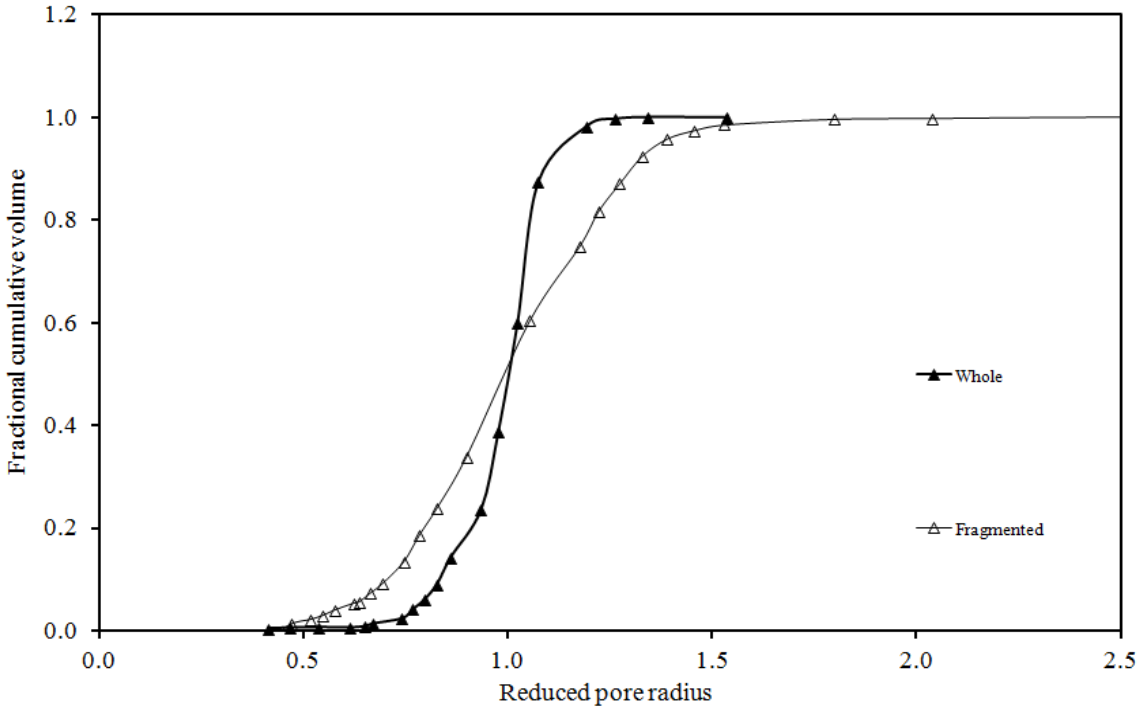

Figure 6.

Reduced pore size distribution obtained from NMR cryoporometry boundary melting curves for fully saturated, whole and fragmented forms of a sample from batch S1.

CONCLUSIONS

It has been seen that the onset, as fractional saturation increases, of particular advanced melting effects of the adsorbed phase can be discerned using NMR cryoporometry. NMR relaxometry and diffusometry data have also shown that the surface area to volume ratio, and the inter-connectivity, of condensate ganglia, decrease, and increase, respectively, at the saturation levels associated with significant onset of advanced melting. It is thus supposed that the onset of advanced melting is associated with a percolation-type transition in the connectivity of the ganglia. The breakdown of the pore-filling process into steps, that can be monitored independently, enables the particular subsets of pores, and their relevant inter-

connections, that control advanced melting to be discerned. This then allows the deduction of which sets of pore sizes are most likely to be either over-represented, or under-estimated, in the PSD.

ACKNOWLEDGEMENTS

The authors are grateful to the University of Bath for the award of a University PhD studentship to ES.

REFERENCES

1. Rouquerol, F., Rouquerol, J., Sing, K., Adsorption by Powders and Porous Solids: Principles, Methodology and Applications. Academic Press, London, 1999.

2. Barrett, E.P., Joyner, L.G., Halenda, P.H. J.Am.Chem.Soc. 73 (1951) 373.

3. Neimark, A.V., Ravikovitch, P.I., Micropor. Mesopor. Mat. 44 (2001) 697.

4. De Boer, J.H. The shapes of capillaries, In The structure and properties of porous solids, Everett, D.H. and F.S. Stone, (Eds.), Butterworths Scientific Publications: London, 1958, p. 68.

5. Cohan, L.H., J. Am. Chem. Soc. 60 (1938) 433.

6. Esparza, J.M.; Ojeda, M.L.; Campero, A.; Dominguez, A.; Kornhauser, I.; Rojas, F.; Vidales, A.M.; López, R.H.; Zgrablich, G., Colloids Surfaces A: Physicochem. Eng. Aspects 241 (2004) 35.

7. Coasne, B.; Galarneau, A.; Di Renzo, F.; Pellenq, R.M.. J. Phys. Chem. C 111 (2007) 15759.

8. Detchverry, F.; Kierlik, E.; Rosinberg, M.L.; Tarjus, G., Langmuir 20 (2004) 8006.

9. Casanova, F.; Chiang, C.E; Li, C.-P.; Schuller, I.K., Appl. Phys. Lett. (2007) 243103.

10 Casanova, F.; Chiang, C.E; Li, C.-P.; Roshschin, I.V.; Ruminski, A.M.; Sailor, M.J.; Schuller, I.K., Nanotechnology 19 (2008) 315709.

11. Giacobbe, F.; Aylmore, L.A.G.; Steele, W.A., J. Colloid Interface Sci. 3 (1972) 277.

12. Hitchcock, I.; Chudek, J.A.; Holt, E.M.; Lowe, J.P.; Rigby, S.P., Langmuir 26 (2010) 18061.

13. Mitchell, J., Webber, J.B.W., Strange, J., Phys. Rep. 461 (2008) 1-36.

14. Jähnert, S.; Vaca Chávez, F.; Schaumann, G.E.; Schreiber, A.; Schönhoff, M.; Findenegg, G.H., Phys. Chem. Chem. Phys. 10 (2008) 6039.

15. Hitchcock, I., Holt, E.M., Lowe, J.P., Rigby, S.P., Chemical Engineering Science 66 (2011) 582.

16. Allen, S.G.; Stephenson, P.C.L.; Strange, J.H., J. Chem. Phys. 108 (1998) 8195.

17. Troyer, W.E.; Holly, R.; Peemoeller, H.; Pintar, M.M., Solid State NMR 28 (2005) 238.

18. Farrher, G.; Ardelean, I.; Kimmich, R., Appl. Magn. Reson. 34 (2008) 85.

19. Naumov, S.; Valiullin, R.; Monson, P.A.; Kärger, J., Langmuir 24 (2008) 6429.

20. Wu, D., Chen, A., and Johnson Jr. C.S., J. Magn. Reson. A 115 (1995) 260.

21. Hollewand, M.P., and Gladden, L.F., Chem. Engng Sci. 50 (1995) 309.

22. Gjerdåker, L., Humborstad Sørland, G., Aksnes, D., Micropor. Mesopor. Mat. 32 (1999) 305.

23. Mitra, P.P., Sen, P.N., Schwartz, L.M., Phys. Rev. B 47 (1993) 8565.

24 Brownstein K.R., Tarr C.E., J. Magn. Reson. 26 (1977) 17.

25. Rigby, S.P.; Chigada, P.I.; Perkins, E.L.; Watt-Smith, M.J.; Lowe, J.P.; Edler, K.J., Adsorption 14 (2008) 289.

26. Perry, R.H.; Green, D.W., Perry's chemical engineers' handbook. McGraw-Hill, New York, USA, 1997.

27. Fukushima, E; Roeder, S.B.W., Experimental Pulse NMR: A Nuts and Bolts Approach. Perseus Books, Reading, Mass, 1981.

28. Khokhlov, A.; Valiullin, R.R.; Stepovich, M.A.; Karger, J., Colloid J. 70 (2008) 507.

29. Petrov, O., Furó, I., Schuleit, M., Domanig, R., Plunkett, M., Daicic, J., Int. J. Pharm. 309 (2006) 157.

30. Strange, J.H, Rahman, M., and Smith, E.G., Phys. Rev. Lett. 71 (1993) 3589.

31. Holz, M., Heil, S.R., Sacco, A., Phys. Chem. Chem. Phys 2 (2000) 4740.

32. Schreiber, A., Ketelsen, I., Findenegg, G.H., Phys. Chem. Chem. Phys 3 (2001) 1185.

33. Grünberg, B.; Emmler, T.; Gedat, E.; Shenderovich, I.; Findenegg, G.H.; Limbach, H.H.; Buntkowsky, G., Chem. Eur. J. 10 (2004) 5689.

34. Vyalikh, A.; Emmler, T.; Grünberg, B.; Xu, Y.; Shenderovich, I.; Findenegg, G.H.; Limbach, H.H.; Buntkowsky, G., Zeitshrift Physikalische Chemie 221 (2007) 155.

35. Rigby, S.; Gladden, L.F., Chem. Engng Sci. 51 (1996) 2263.

FIGURE CAPTIONS

Figure 1.

(a) Normalized water adsorption (●) and desorption (o) isotherms for a sample of 30 pellets from batch S1, obtained at 294 K. The water uptake was measured gravimetrically. (b) Comparison of adsorption isotherm obtained gravimetrically for 30 pellets (●) with that obtained by NMR for one pellet (■) of Sample 1. The line shown is to guide the eye.

Figure 2.

(a) NMR cryoporometry melting curves for the adsorbed phase in a single pellet sample of S1 (Sample 1) at different relative pressures of water vapour. The inset shows a close-up view of the steep parts of the melting curves for relative pressures of 0.91 and 0.92. The lines shown are to guide the eye. (b) PSDs derived from the melting curve in (a) for a relative pressure of 0.91, and the melting curve for a relative pressure of 1.0, and, also, the PSD derived from nitrogen adsorption using the BJH algorithm.

Figure 3

NMR boundary (solid symbols) freezing and melting curves, and scanning loops (open symbols), obtained for a single pellet sample of S1 (Sample 2) at two different relative pressures (0.92 (triangles) and 1.0 (diamonds)) of water vapour. The lines shown are to guide the eye.

Figure 4.

Variation of NMR spin-spin relaxation time (T_2) for the adsorbed phase, obtained at the top of the melting curves (all at 273 K), with relative pressure (P/P_0) of water vapour for the

sample of S1 used to obtain the data in Figure 2 (Sample 1). The errors in the T_2 values are smaller than the size of the symbols.

Figure 5.

Variation of unrestricted diffusion tortuosity for the adsorbed phase, obtained at the top of the melting curves (all at 273 K), with relative pressure (P/P_0) of water vapour for the sample of S1 used to obtain the data in Figure 2 (Sample 1).

Figure 6.

Reduced pore size distribution obtained from NMR cryoporometry boundary melting curves for fully saturated, whole and fragmented forms of a sample from batch S1.

TABLE CAPTIONS

Table 1.

Results of 2-component fit to the T_2 data obtained at various positions around the scanning loops shown in Figure 3.

Table 2.

Results of PFG NMR experiments, and 1- and 2-component fits to the T_2 data, obtained at some points on the boundary melting curves, obtained at different condensate saturations, for Sample 2.

FIGURE 1.

(a)

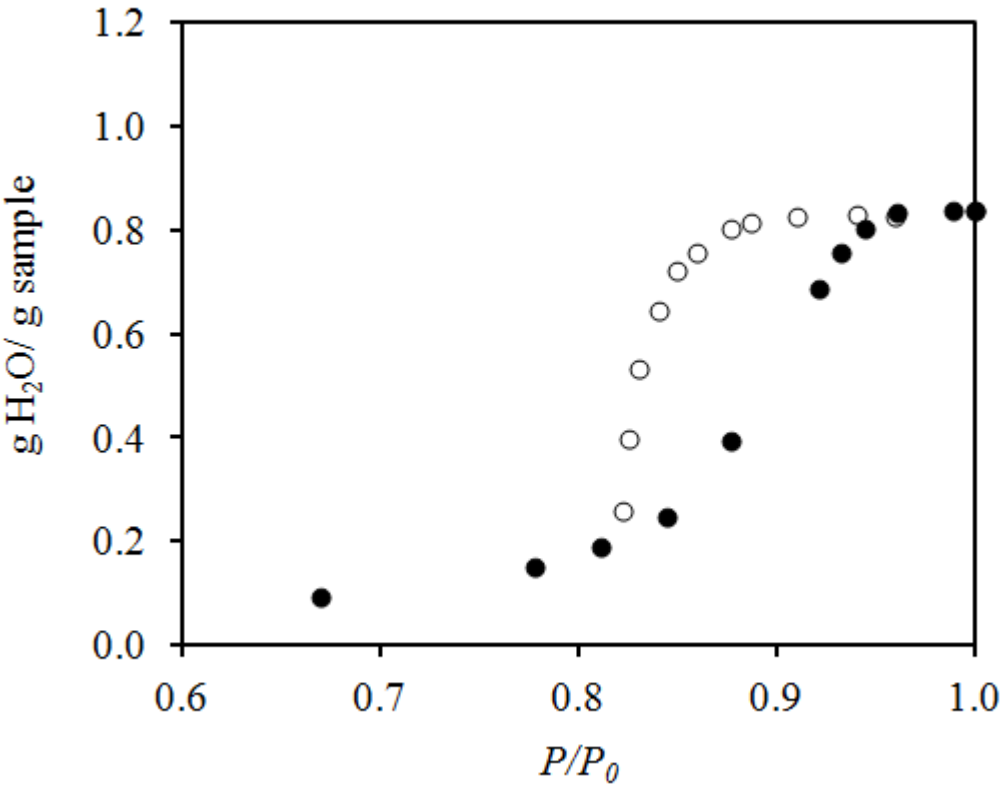

(b)

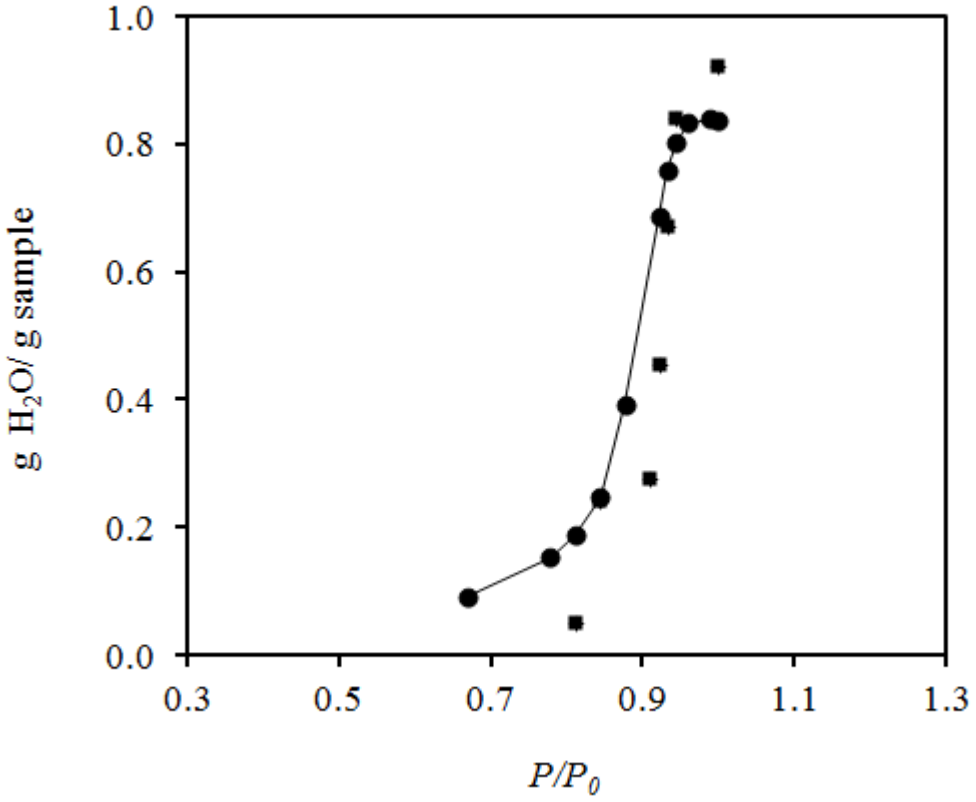

FIGURE 2.

(a)

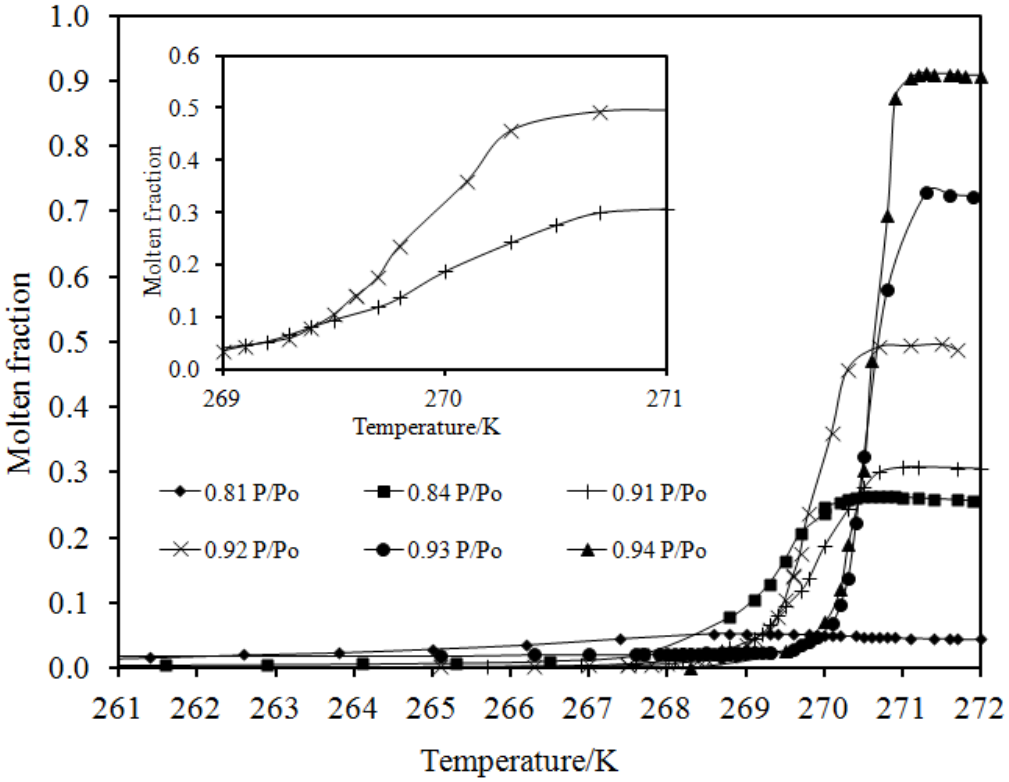
Molten fraction
Temperature/K
0.81 P/Po
0.84 P/Po
0.91 P/Po
0.92 P/Po
0.93 P/Po
0.94 P/Po
Molten fraction
Temperature/K

2 (b)

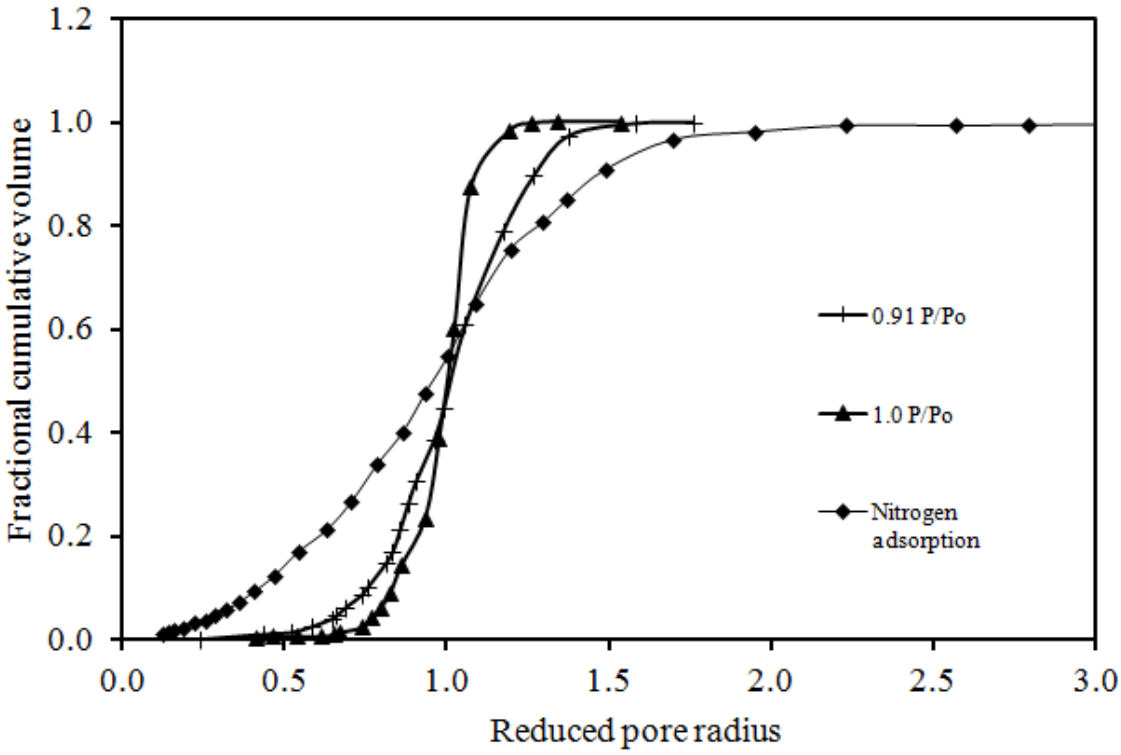
1.2
1.0
0.8
0.6
0.4
0.2
0.0
Fractional cumulative volume
0.0
0.5
1.0
1.5
2.0
2.5
3.0
Reduced pore radius
0.91 P/Po
1.0 P/Po
Nitrogen adsorption

FIGURE 3.

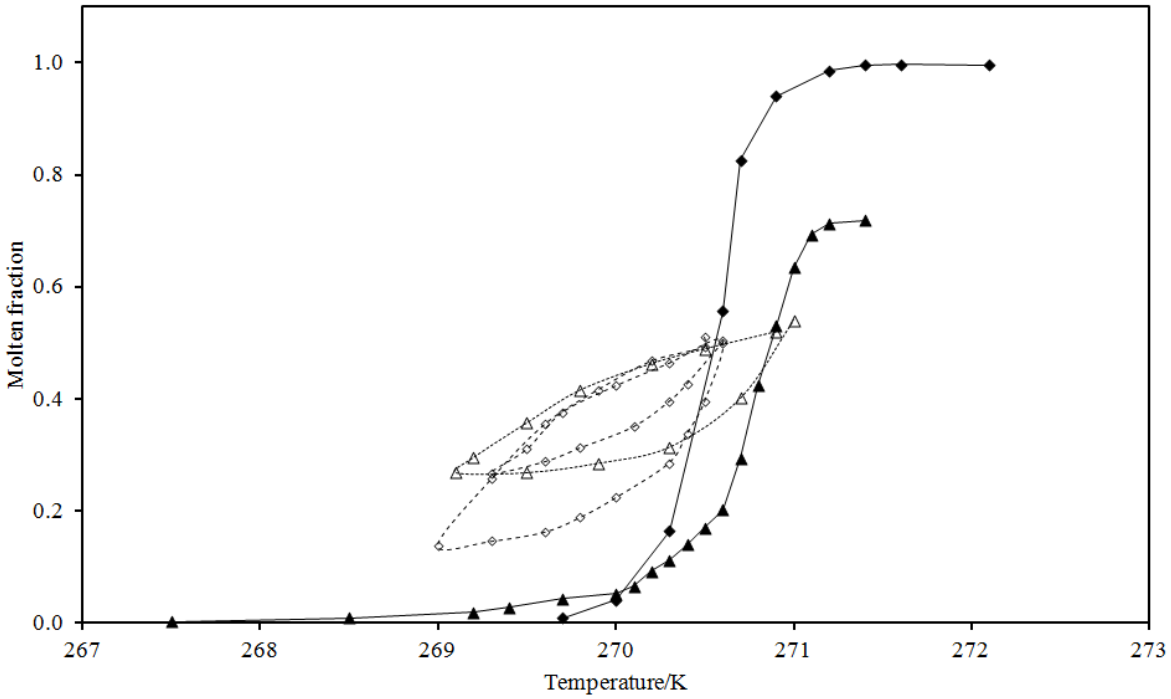
1.0
0.8
0.6
0.4
0.2
0.0
Molten fraction
267
268
269
270
271
272
273
Temperature/K

FIGURE 4

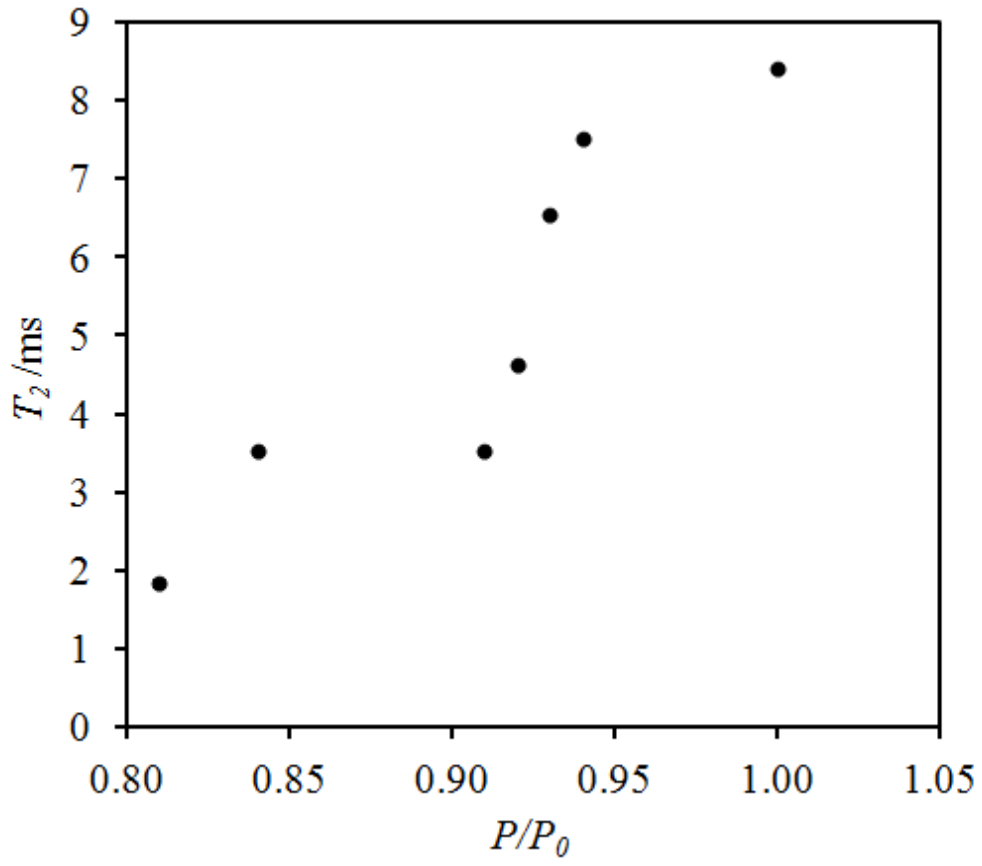

FIGURE 5.

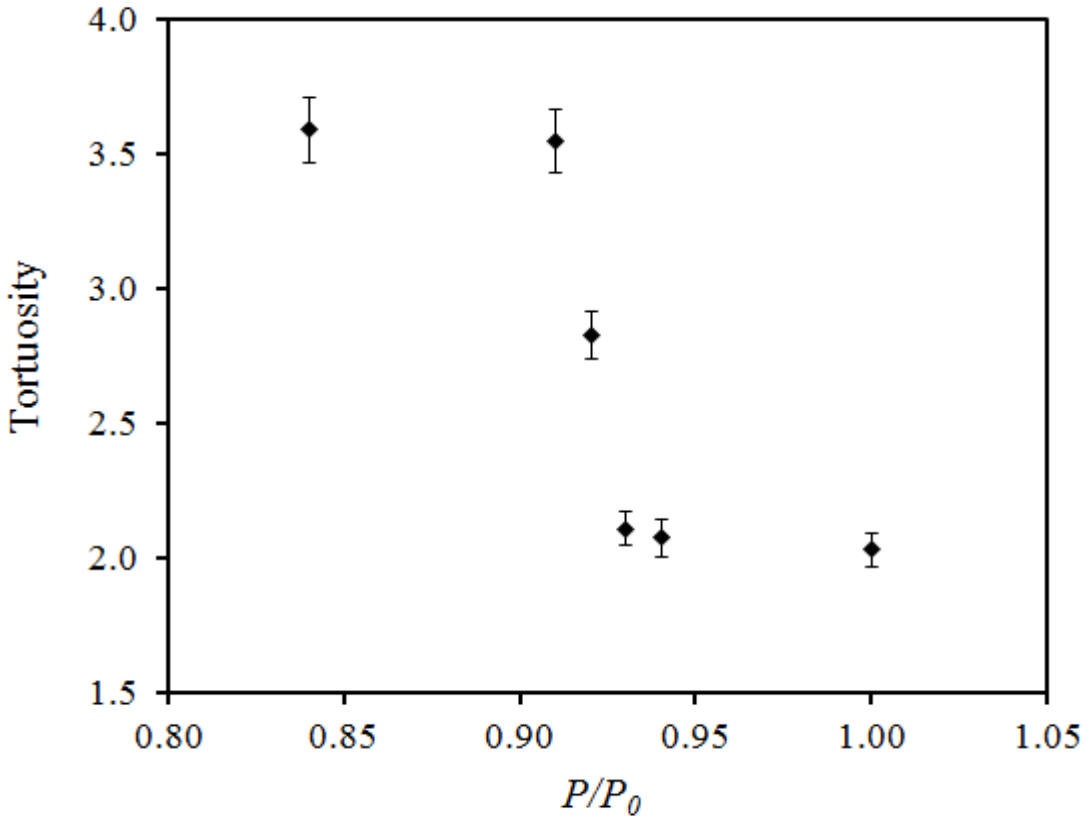

FIGURE 6.

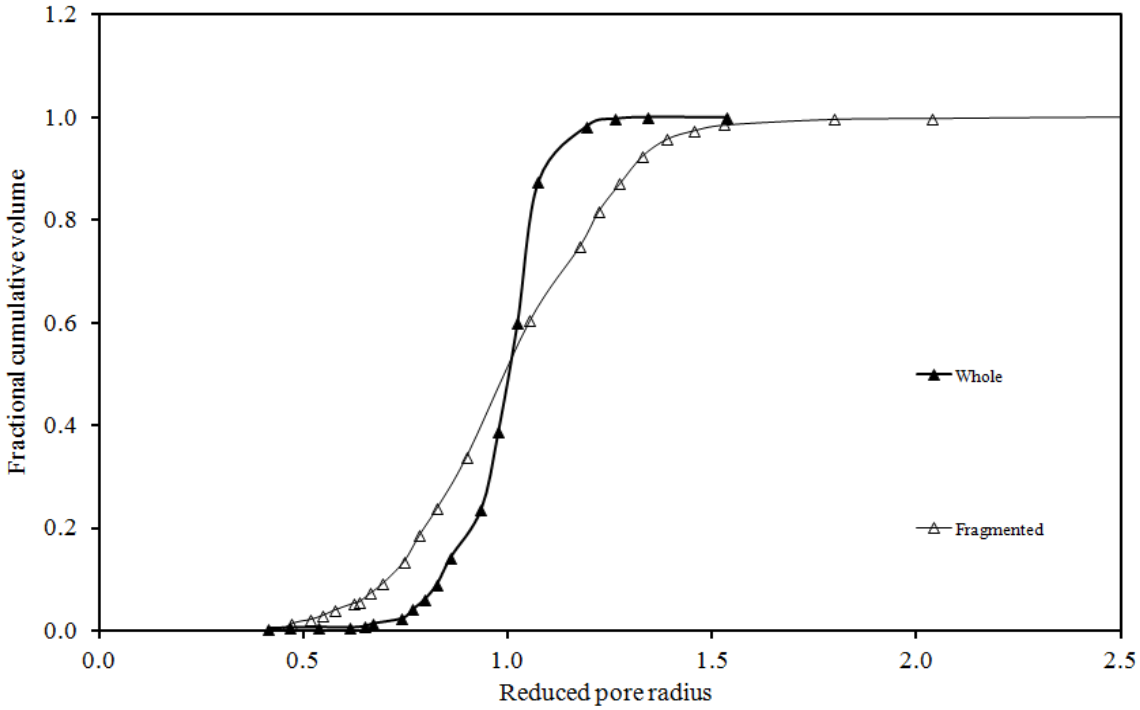
1.2
1.0
0.8
0.6
0.4
0.2
0.0
Fractional cumulative volume
0.0
0.5
1.0
1.5
2.0
2.5
Reduced pore radius
Whole
Fragmented

TABLE 1

Relative pressure	**Loop position**	**T_2 slow component /ms**	**Volume fraction of slow component**	**T_2 fast component /ms**	**Volume fraction of fast component**	**Volume-weighted average T_2/ms**
0.92	Top	4.5	0.33	0.3	0.67	4.3±0.3
1.0	Top	5.5	0.45	2.1	0.55	3.6±0.1
0.92	Bottom	2.8	0.33	0.5	0.67	2.1±0.1
1.0	Bottom (equal temperature to 0.92 loop)	1.9	0.39	1.1	0.61	1.06±0.01
1.0	Bottom (equal molten fraction to 0.92 loop)	2.6	0.51	0.7	0.49	2.1±0.1

TABLE 2.

Relative pressure	**Molten volume fraction**	**Tortuosity**	T_2**/ms**
0.92	0.72	2.25±0.07	7.6±0.2[a]
1.0	1.0	1.82±0.05	9.95±0.02[a]
1.0	0.72	1.86±0.06	4.6±0.1[a,b]

Notes: [a] 1-component fit, [b] 2-component fit gives same mean as 1-component

Appendix

Figure A1 shows an example of a log-attenuation plot for the data from a T_2 relaxometry experiment, from the partially saturated at relative pressure 0.84. Fig. A2 shows an example of a log-attenuation plot of a PFG-NMR experiment. Both graphs show monoexponential decay, implying that there is no exchange between the liquid and vapour phase of water within the pores, at the very low saturation levels.

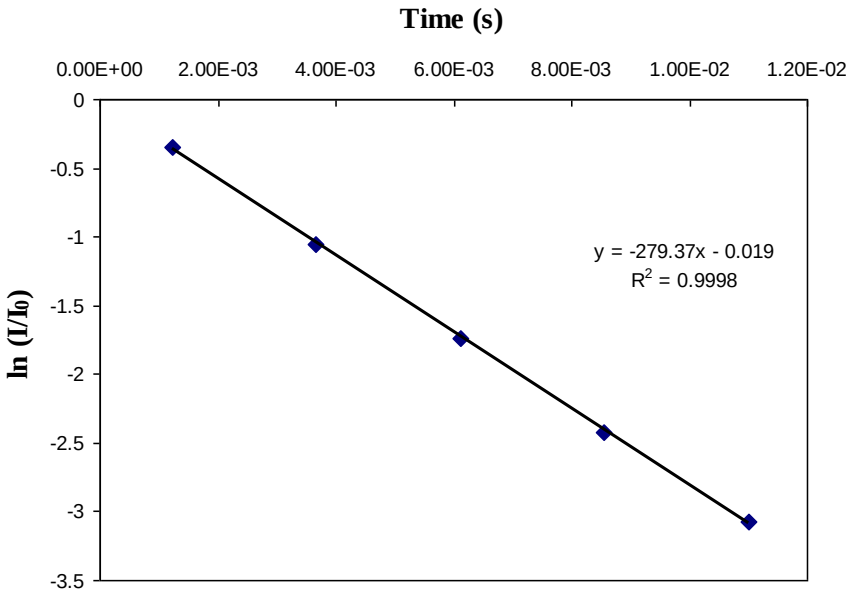

Figure A1. Log-attenuation plot of data (diamonds) from a T_2 relaxation experiment conducted on the 100 % molten fraction of the single S1 pellet, at 273 K. The sample was saturated at relative pressure 0.84, at 294 K. The solid line shows the fit to equation 4

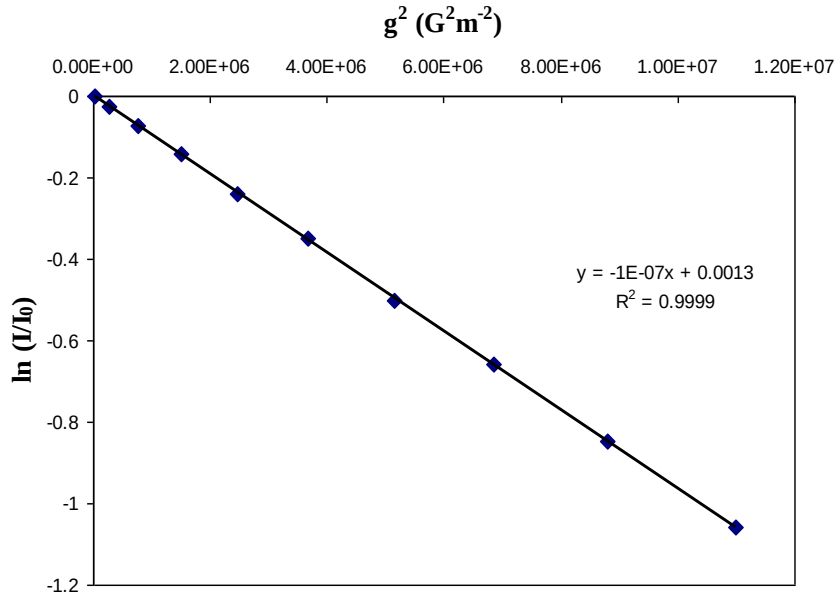

Figure A2. Log-attenuation plot of data from a PFG experiment, at 100% molten fraction, at 273 K, saturated at the low relative pressure of 0.84. Δ=0.15 s and δ= 0.002 s. The raw data (diamonds) were fitted to equation 1.

For Table of Contents Only